Upper-Ocean Processes under the Stratus Cloud Deck in the Southeast Pacific Ocean

Yangxing Zheng,* Toshiaki Shinoda,[+] George N. Kiladis,* Jialin Lin,[#] E. Joseph Metzger,[+] Harley E. Hurlburt,[+] and Benjamin S. Giese[@]

* NOAA/ESRL/CIRES Climate Diagnostics Center, Boulder, Colorado
[+] Naval Research Laboratory, Stennis Space Center, Mississippi
[#] Department of Geography, The Ohio State University, Columbus, Ohio
[@] Department of Oceanography, Texas A&M University, College Station, Texas

ABSTRACT

The annual mean heat budget of the upper ocean beneath the stratocumulus/stratus cloud deck in the southeast Pacific is estimated using Simple Ocean Data Assimilation (SODA) and an eddy-resolving Hybrid Coordinate Ocean Model (HYCOM). Both are compared with estimates based on Woods Hole Oceanographic Institution (WHOI) Improved Meteorological (IMET) buoy observations at 20°S, 85°W. Net surface heat fluxes are positive (warming) over most of the area under the stratus cloud deck. Upper-ocean processes responsible for balancing the surface heat flux are examined by estimating each term in the heat equation. In contrast to surface heat fluxes, geostrophic transport in the upper 50 m causes net cooling in most of the stratus cloud deck region. Ekman transport provides net warming north of the IMET site and net cooling south of the IMET site. Although the eddy heat flux divergence term can be comparable to other terms at a particular location, such as the IMET mooring site, it is negligible for the entire stratus region when area averaged because it is not spatially coherent in the open ocean. Although cold-core eddies are often generated near the coast in the eddy-resolving model, they do not significantly impact the heat budget in the open ocean in the southeast Pacific.

1. Introduction

Sea surface temperature (SST) in the southeast Pacific near the coasts of Peru and Chile is colder than at any comparable latitude elsewhere. It is believed that these cold waters in the southeast Pacific play an important role in the formation and maintenance of persistent stratocumulus/stratus cloud decks and that these clouds have a significant impact on regional and global climate (e.g., Ma et al. 1996; Miller 1997; Gordon et al. 2000; Xie 2004). Thus, it is important to understand upper-ocean processes that maintain SST under the stratocumulus cloud deck for global simulation and climate prediction. However, until recently, the upper ocean in this region has been sparsely observed, which limits our ability to better understand and simulate the behavior of the at-

mosphere and ocean globally. In fact, most atmosphere–ocean coupled general circulation models (CGCMs) have systematic errors in the southeast Pacific, including too warm SSTs and too little cloud cover (e.g., Mechoso et al. 1995; Ma et al. 1996; Lin 2007), which have important impacts on the simulated radiation budget and climate sensitivity.

As part of the Eastern Pacific Investigation of Climate (EPIC), a well-instrumented surface mooring was deployed under the middle of the stratus cloud deck (20°S, 85°W) in October 2000, providing 6 yr of upper-ocean temperature, salinity, velocity, and surface meteorological variables (Colbo and Weller 2007). Using these datasets as well as other satellite and historical data, Colbo and Weller (2007) estimated the upper-ocean heat budget (upper 250 m) at the location of the mooring to understand upper-ocean processes that maintain the annual mean heat content of the upper ocean in this region. They found that the major terms of the heat equation that balance positive (warming) surface heat fluxes are geostrophic heat transport and eddy heat flux divergence.

Corresponding author address: Yangxing Zheng, NOAA/ESRL/CIRES Climate Diagnostics Center, 325 Broadway, R/PSD1, Boulder, CO 80305.
E-mail: yangxing.zheng@noaa.gov

Report Documentation Page		*Form Approved* *OMB No. 0704-0188*

Public reporting burden for the collection of information is estimated to average 1 hour per response, including the time for reviewing instructions, searching existing data sources, gathering and maintaining the data needed, and completing and reviewing the collection of information. Send comments regarding this burden estimate or any other aspect of this collection of information, including suggestions for reducing this burden, to Washington Headquarters Services, Directorate for Information Operations and Reports, 1215 Jefferson Davis Highway, Suite 1204, Arlington VA 22202-4302. Respondents should be aware that notwithstanding any other provision of law, no person shall be subject to a penalty for failing to comply with a collection of information if it does not display a currently valid OMB control number.

1. REPORT DATE **28 JUL 2009**	2. REPORT TYPE	3. DATES COVERED **00-00-2009 to 00-00-2009**
4. TITLE AND SUBTITLE **Upper-Ocean Processes under the Stratus Cloud Deck in the Southeast Pacific Ocean**		5a. CONTRACT NUMBER
		5b. GRANT NUMBER
		5c. PROGRAM ELEMENT NUMBER
6. AUTHOR(S)		5d. PROJECT NUMBER
		5e. TASK NUMBER
		5f. WORK UNIT NUMBER
7. PERFORMING ORGANIZATION NAME(S) AND ADDRESS(ES) **Naval Research Laboratory,Stennis Space Center,MS,39529**		8. PERFORMING ORGANIZATION REPORT NUMBER
9. SPONSORING/MONITORING AGENCY NAME(S) AND ADDRESS(ES)		10. SPONSOR/MONITOR'S ACRONYM(S)
		11. SPONSOR/MONITOR'S REPORT NUMBER(S)

12. DISTRIBUTION/AVAILABILITY STATEMENT **Approved for public release; distribution unlimited**

13. SUPPLEMENTARY NOTES

14. ABSTRACT **see report**

15. SUBJECT TERMS

16. SECURITY CLASSIFICATION OF:			17. LIMITATION OF ABSTRACT **Same as Report (SAR)**	18. NUMBER OF PAGES **19**	19a. NAME OF RESPONSIBLE PERSON
a. REPORT **unclassified**	b. ABSTRACT **unclassified**	c. THIS PAGE **unclassified**			

Standard Form 298 (Rev. 8-98)
Prescribed by ANSI Std Z39-18

Based on the results of their analysis, they hypothesized that cooling resulting from the eddy heat flux divergence is a result of westward propagation of cold coherent eddies formed near the coast that slowly decay in the open ocean.

Although the analysis of Colbo and Weller (2007) at the Improved Meteorological (IMET) site significantly improved our understanding of the upper ocean in this region, a variety of assumptions were made in their estimates, because it is difficult to calculate all terms in the heat equation from the data at one location. In particular, the eddy heat flux divergence was estimated as a residual from the closure of the heat budget in the heat equation. Although the estimates for the upper 250-m layer help understand processes that control the upper-ocean heat content, SSTs may not be directly affected by advection and eddy fluxes around 250-m depth because the deepest mixed layer depth during winter is ~150 m. Furthermore, the persistent stratus cloud decks occupy a large portion of southeast Pacific (Klein and Hartmann 1993; Colbo and Weller 2007), and it is difficult to identify important upper-ocean processes for the entire stratus region from an analysis of one location.

In this study, three-dimensional upper-ocean processes for the entire stratus cloud region are examined using Simple Ocean Data Assimilation (SODA; Carton and Giese 2008) and an eddy-resolving ocean general circulation model (OGCM): the Hybrid Coordinate Ocean Model (HYCOM). The datasets obtained from the mooring observations are utilized to evaluate the model performance. The annual mean of the terms contributing to the heat budget are calculated at the mooring site and compared with observational estimates. Contributing terms are also estimated for the entire stratus cloud deck region to examine the representativeness of the mooring site for broadscale upper-ocean processes. In addition, terms contributing to the heat budget in the upper 50 m are computed from the model output to improve our understanding of upper-ocean processes that control sea surface temperature variability in this region. In particular, the relative importance of horizontal heat advection and eddy heat flux divergence in the upper-ocean heat budget is emphasized, and the role of cold-core eddies generated near the coast in the open ocean heat budget is also discussed.

2. Models and datasets

a. SODA

The SODA methodology, the ingested data, and the error covariance structure of both the model and the observations are described by Carton et al. (2000a,b), Carton and Giese (2008), and Zheng and Giese (2009). The ocean model is based on the Los Alamos implementation of the Parallel Ocean Program (POP; Smith et al. 1992). The model resolution is on average $0.4° \times 0.25°$ (longitude $\times$ latitude) with 40 levels in the vertical. The model is forced with the 40-yr European Centre for Medium-Range Weather Forecasts (ECMWF) Re-Analysis (ERA-40) daily atmospheric reanalysis winds (Simmons and Gibson 2002) for the 44-yr period from 1958 to 2001. We update the analysis in a second run forced by Quick Scatterometer (QuikSCAT) wind stress from 2002 to 2005.

Surface heat fluxes are computed from bulk formulae (Smith et al. 1992), with atmospheric variables that come from the National Centers for Environmental Prediction–National Center for Atmospheric Research (NCEP–NCAR) reanalysis (Kalnay et al. 1996). The NCEP–NCAR reanalysis information is used for the bulk formulas instead of the ERA-40 variables throughout the experiment to give continuity of surface forcing during periods for which the ERA-40 winds are not available. However, the details of surface heat flux boundary condition are relatively unimportant in influencing the solution, because near-surface temperature observations are used to update the mixed layer temperature. Vertical diffusion of momentum, heat, and salt is based on a nonlocal K-profile parameterization (KPP; Large et al. 1994) scheme and horizontal diffusion for subgrid-scale processes is based on a biharmonic mixing scheme.

The model is constrained by observed temperature and salinity, using a sequential assimilation algorithm, which is described by Carton et al. (2000a,b) and Carton and Giese (2008). The basic subsurface temperature and salinity observation sets consist of approximately 7×10^6 profiles, of which two-thirds have been obtained from the World Ocean Database 2001 (Boyer et al. 2002; Stephens et al. 2002) with online updates through December 2004. This dataset has been extended by the addition of real-time temperature profile observations from the Tropical Atmosphere Ocean/Triangle Trans-Ocean Buoy Network (TAO/TRITON) mooring thermistor array and Argo floats. In addition to the temperature profile data, a large number of near-surface temperature observations are available both in the form of in situ observations [bucket and ship-intake temperatures from the Comprehensive Ocean-Atmosphere Dataset (COADS) surface marine observation set of Diaz et al. (2002)] and from satellite remote sensing. SODA used the nighttime National Oceanic and Atmospheric Administration–National Aeronautics and Space Administration (NOAA–NASA) Advanced Very High Resolution Radiometer (AVHRR) operational SST data, which began November 1981 and average 25 000 samples per week. Use of only nighttime

retrievals reduces the error resulting from skin temperature effects. However, the biggest challenge in retrieving SST from an infrared (IR) instrument in the southeast Pacific Ocean is the cloud detection problem, because clouds are opaque to infrared radiation and can effectively mask radiation from the ocean surface. Carton et al. (2000a,b) used a bias-corrected model error covariance in an attempt to reduce such error. The near-surface salinity observation set averages more than 10^5 observations per year since 1960 (Bingham et al. 2002). Nearly continuous sea level information is available from a succession of altimeter satellites beginning in 1991. Although the coverage of subsurface data in the southeast Pacific Ocean is not as good as other regions in the tropics, a significant amount of satellite observations are used in SODA, especially after 1980 (not shown). The yearly number of observations in the southeast Pacific (35°–5°S, 140°–70°W) exceeds 10^5 after 1984. Hence, it is likely that SODA analysis can provide more accurate estimates of mean heat advection than models with no data assimilation.

Averages of model output variables (temperature, salinity, and velocity) are saved at 5-day intervals. These average fields are remapped onto a uniform global 0.5° × 0.5° horizontal grid using the horizontal grid spherical coordinate remapping and interpolation package with second-order conservative remapping (Jones 1999).

b. HYCOM

HYCOM was developed from the Miami Isopycnic Coordinate Ocean Model using the theoretical foundation set forth in Bleck and Boudra (1981), Bleck and Benjamin (1993), and Bleck (2002). A description of the recent version of global HYCOM used in this study can be found in Hurlburt et al. (2008). HYCOM uses a generalized vertical coordinate that is normally isopycnal in the open stratified ocean; makes a dynamically smooth transition to pressure coordinates (nearly z level) in the mixed layer and other unstratified or weakly stratified water and to σ (terrain following) coordinates in shallow water, although it is not limited to these coordinate choices. Another key feature of HYCOM is that it can have zero thickness layers, allowing isopycnals to intersect sloping topography. Where HYCOM uses pressure coordinates, partial cell topography is an automatic consequence of the generalized vertical coordinate design. The system is configured for the global ocean with HYCOM 2.2 as the dynamical model. Computations are carried out on a Mercator grid between 78°S and 47°N with a horizontal resolution of $1/12°$ × $1/12°$ cos(latitude). North of 47°N, the global model grid is a bipolar cap with the singularities placed over Asia and North America. There are 32 layers in the vertical. Bottom topography is derived from a quality-controlled Naval Research Laboratory (NRL) Digital Bathymetry Data Base with 2-min resolution (DBDB2) dataset. Three-hourly surface forcing is from the Navy Operational Global Atmospheric Prediction System (NOGAPS; Rosmond et al. 2002) and includes wind stress, wind speed, heat flux (using bulk formula; Kara et al. 2005a), and precipitation.

HYCOM uses a penetrating solar radiation scheme that accounts for the effects of spatial and temporal variations in water turbidity (Kara et al. 2005b). This scheme is designed to improve the simulation of upper-ocean quantities, especially SST. The net longwave flux is the sum of downward longwave (from the atmosphere) and upward blackbody radiation. The blackbody radiation from ERA-40 is corrected to allow for the difference between ERA-40 SST and HYCOM SST (Kara et al. 2005c). Latent and sensible heat fluxes at the air–sea interface are computed using efficient and accurate bulk parameterizations (Kara et al. 2005a).

As in SODA, KPP is used for vertical mixing in the model. Global HYCOM was integrated for the time period from January 2003 to April 2007. During this period, the tropical Pacific Ocean was in a near-normal condition with no strong El Niño and La Niña events. In this study, model output from HYCOM is used primarily for identifying the role of eddies in the heat budget of the upper ocean under the stratus cloud deck in the southeast Pacific.

c. Datasets

The dataset used in this study is from a well-instrumented IMET buoy developed at the Woods Hole Oceanographic Institution (WHOI) and deployed at 20°S, 85°W in October 2000. Six years of high-quality data (8 October 2000–18 October 2006) were used here. The surface heat fluxes are calculated using SST and surface meteorological variables from the IMET buoy using the Tropical Ocean Global Atmosphere Coupled Ocean–Atmosphere Response Experiment (TOGA COARE) bulk air–sea flux algorithm version 2.6 (Bradley et al. 2000). More detailed description of IMET datasets can be found in Colbo and Weller (2007). *The World Ocean Atlas 2005* (WOA05) monthly temperature and salinity climatology is also used for determining uncertainties in the model's annual mean horizontal heat advection. The gridded ($1/3°$ × $1/3°$, Mercator grid) product of Ocean Topography Experiment (TOPEX)/Poseidon, *European Remote Sensing Satellite-1* (*ERS-1*) and *ERS-2*, and *Jason-1* and *Jason-2* sea surface heights and geostrophic currents (computed from absolute topography) produced by Segment Sol Multimissions d'Altimétrie, d'Orbitographie et de Localisation Précise/Data Unification and Altimeter Combination System (SSALTO/DUACS) and
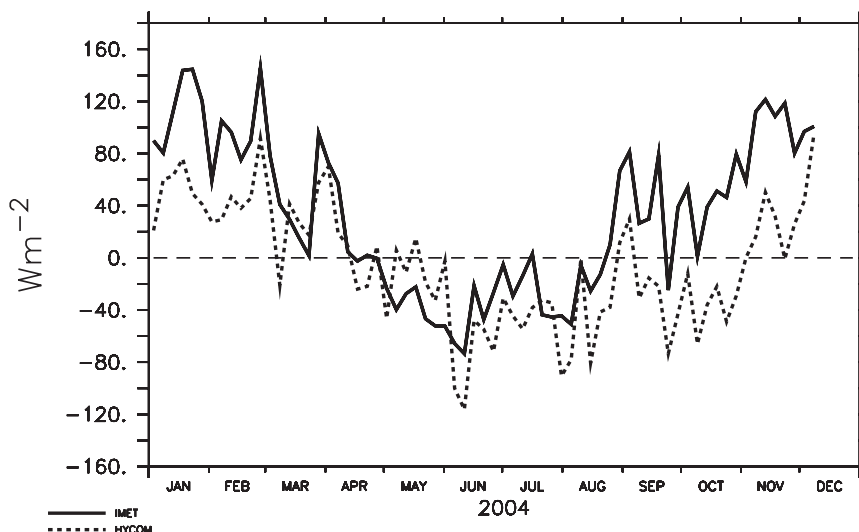
FIG. 1. Time series of 5-day-mean net surface heat flux (W m^{-2}; upward positive) from WHOI IMET measurements (solid line) and estimates based on NOGAPS and HYCOM's SST (dashed line) during 3 Jan–8 Dec 2004. The zero lag correlation coefficient between the data and HYCOM in 2004 is 0.78.

distributed by Archiving, Validation, and Interpretation of Satellite Oceanographic data (AVISO) are used to validate the model's ability to simulate eddy activity. The dataset spans 22 August 2001–28 February 2009.

3. Comparisons with the IMET observations

We first compare the surface heat flux used to force HYCOM and subsurface temperature in SODA and HYCOM with those from the IMET buoy observations at 20°S, 85°W. Note that surface heat fluxes used for SODA are not available.

a. Surface heat flux

Figure 1 shows the time series of the 5-day-averaged net surface heat flux estimates at (20°S, 85°W) for HYCOM and the IMET observations spanning 3 January 2004–8 December 2004. The net surface heat flux is computed based on the shortwave radiation, longwave radiation, and surface sensible and latent heat fluxes from NOGAPS atmospheric variables and HYCOM SST. The seasonal variation of surface heat flux based on NOGAPS agrees with the IMET estimate reasonably well (correlation coefficient = 0.78). However, there are significant differences between estimates based on the IMET and NOGAPS. For example, during January–early February and September–November, IMET estimates are larger by ~80 W m^{-2}. The root-mean-square (RMS) difference is 53 W m^{-2} using the 5-day means over this period. Because of these discrepancies, the mean surface heat

flux from IMET observations is significantly larger (Table 1). Nevertheless, as will be discussed in section 4a, the net surface heat fluxes based on NOGAPS are positive (warming) in most areas discussed in this study, which is consistent with the IMET estimate. To further confirm the spatial distribution of surface heat flux in this region, we have examined the annual mean heat fluxes in the Objectively Analyzed Air-Sea Fluxes (OAFlux; Yu and Weller 2007; Yu et al. 2008) and other atmospheric reanalyses [NCEP–NCAR Global Reanalysis 1 (NCEP-1), NCEP-2, and ERA-40]. All datasets show the net surface heat fluxes are positive in most of the stratus region (not shown). Hence, the surface heat flux estimates based on NOGAPS are suitable for driving the HYCOM in this study, which primarily examines upper-ocean processes that balance the positive surface heat fluxes in the stratus region.

TABLE 1. Comparison between Colbo and Weller's estimates based on the IMET buoy datasets (0–250 m) and the models (0–250 m) in the upper-ocean heat budget. The periods for the averaging are October 2000–December 2004 for Colbo and Weller's (2007) estimates, January 1980–November 2005 for SODA, and January 2003–April 2007 for HYCOM (units are W m^{-2}).

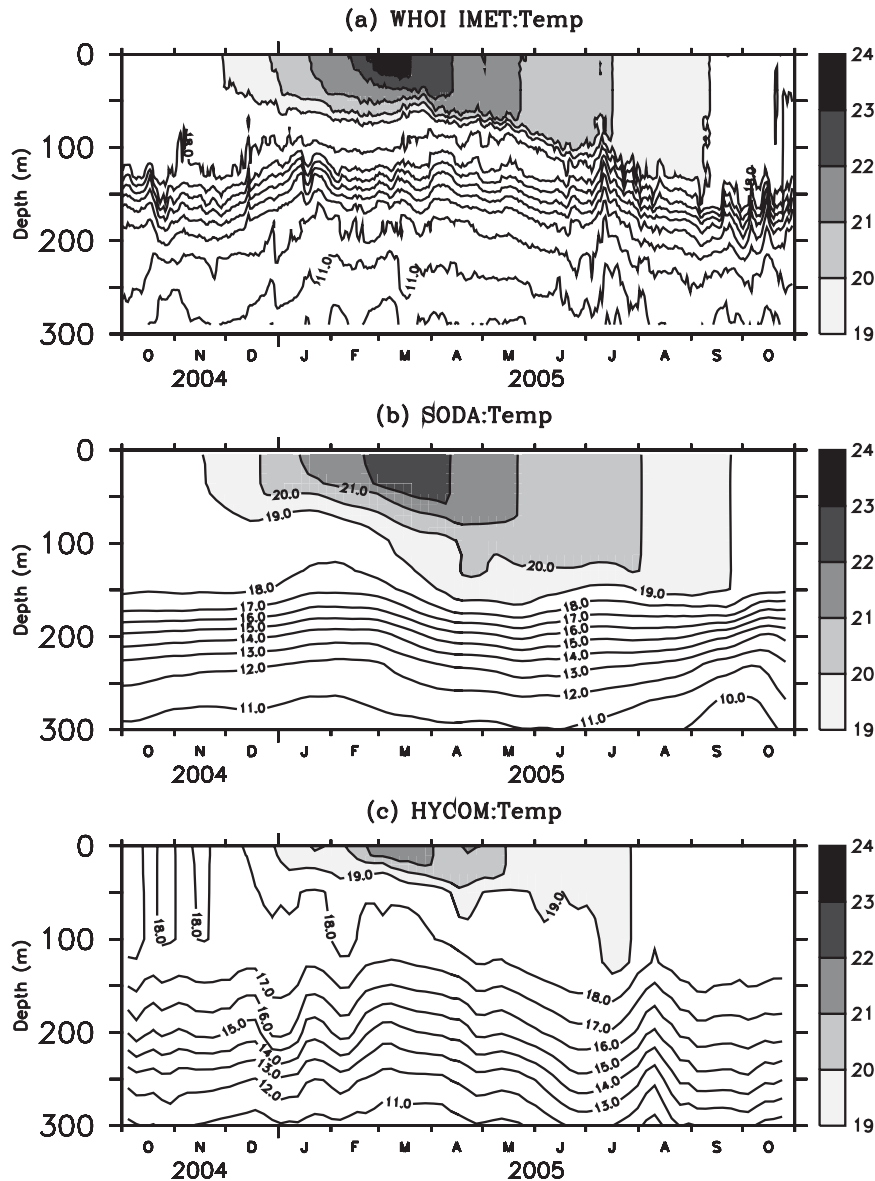| (20°S, 85°W)	Q_{net}	$-\mathbf{V}_{geo} \cdot \nabla T$	$-\mathbf{V}_{ek} \cdot \nabla T$	$-\nabla \cdot (\overline{\mathbf{V}'T'})$
Colbo and Weller (2007)	44	−20	6	−30
SODA	—	−21	11	−19
HYCOM	18	−45	−44	42

FIG. 2. (a) Daily mean temperature of the upper 300 m at (20°S, 85°W) during 1 Oct 2004–
31 Oct 2005 from WHOI IMET measurements. Five-day mean temperatures of the upper 300 m
during the same period from (b) SODA and (c) HYCOM. The contour interval is 1°C.

b. Upper-ocean temperature

Model simulations of tropical oceans using HYCOM
were previously evaluated by comparing with in situ and
satellite observations (Shaji et al. 2005; Han 2005; Han
et al. 2006; Shinoda et al. 2008; Shinoda and Lin 2009).
These studies show HYCOM is able to simulate upper-
ocean variability reasonably well, including that within
the stratus cloud deck region.

Figure 2 shows the temperature evolution in the upper
300 m from IMET observations, and from the nearest

grid points in SODA and HYCOM over 1 October
2004–31 October 2005. Both SODA and HYCOM are
able to capture the seasonal evolution of the mixed layer,
in which the mixed layer depth is about 20–30 m in the
austral summer (February–March) and becomes deepest
(~150 m) after the austral winter (September–October).
The thermocline structure is better reproduced in SODA
than HYCOM. This is because observational data were not
assimilated into the HYCOM simulation. Nevertheless,
given that seasonal evolution of the mixed layer (above
~150 m) is well reproduced by models, these experiments

are suitable for this study, which primarily discusses estimates of the heat budget in the upper 50 m. It should be noted that the agreement between models and observations in other years is similar to this period (not shown).

c. Mean heat budget

The heat equation integrated over several years and down to some depth z_0 is

$$\int_0^{\text{years}} \int_{z_0}^0 \frac{\partial T}{\partial t}\, dz\, dt = \int_0^{\text{years}} \left\{ \frac{Q_{\text{net}}}{C_p \rho} - \int_{z_0}^0 \left[\mathbf{V} \cdot \nabla_h T + w\frac{\partial T}{\partial z} + \nabla \cdot (\overline{\mathbf{V}'T'}) + \kappa_h \nabla^2 T \right] dz - \kappa_v \frac{dT}{dz}\bigg|_{z_0} \right\} dt,$$

where Q_{net} is the net surface heat flux, C_p is the specific heat of seawater at constant pressure, ρ is the density of seawater, w is the vertical velocity, $\mathbf{V}$ is horizontal velocity vector, T is temperature, and $\mathbf{V}'$ and T' are deviations from the seasonal mean. Here, z_0 is assumed to be deep enough so that the penetrative component of shortwave radiation is within the layer, and $\nabla \cdot (\overline{\mathbf{V}'T'})$ on the right-hand side is the divergence of eddy heat flux. The time scale of the mean has to be defined to calculate this term. Following some previous studies (Penven et al. 2005; Colbo and Weller 2007), we use the seasonally averaged velocity and temperature ($\sim$90-day averages) as the mean values in this study. Accordingly, $\mathbf{V}$, w, and T are the seasonally averaged values from 5-day-averaged data. The first term on the left-hand side is the rate of temperature change (or temperature tendency), which is negligible when averaged over several years. The terms on the right-hand side are net surface heat flux, horizontal heat advection, vertical heat advection, divergence of eddy heat flux, and horizontal and vertical diffusion, respectively. In this study, horizontal advection and the divergence of eddy heat flux are the primary focus of the discussion. Colbo and Weller (2007) suggest that these terms are important and they can be reliably estimated from the model output. Note that some of the other terms are difficult to estimate from the model output because of variable unavailability and the errors resulting from coordinate transformation and interpolations.

Table 1 shows the mean heat flux resulting from geostrophic and Ekman currents and eddy heat flux divergence in the upper 250 m at 20°S, 85°W from the models and Colbo and Weller's (2007) estimates based on IMET datasets. The numbers of Colbo and Weller's estimates in this table are obtained directly from their paper (Colbo and Weller 2007). The periods for the averaging are October 2000–December 2004 for Colbo and Weller's (2007) estimates, January 1980–November 2005 for SODA, and January 2003–April 2007 for HYCOM. We note that the eddy flux divergence was computed as a residual in Colbo and Weller (2007). Geostrophic currents are computed from the model temperature and salinity. Ekman currents are calculated from the difference between geostrophic and total velocities. This approximation will be discussed in section 4c. Although it is unlikely that quantitative agreement of these estimates would be found at one location because of the variety of assumptions made for the observational estimates, model deficiencies, and the errors in the surface forcing fields, it is noteworthy that some of the terms estimated from the models are reasonably consistent with the Colbo and Weller estimates. For instance, the cold advection resulting from geostrophic transport in SODA and HYCOM is comparable to their estimates. Heat advection resulting from Ekman transport in SODA is also consistent with their estimates. Eddy flux divergence is large at the IMET site in the Colbo and Weller estimates as well as in the models, though HYCOM gives a positive sign. The difference in geostrophic heat transport is mostly due to the zonal component of geostrophic currents and the meridional temperature gradient (not shown).

To examine the representativeness of the mooring observations at a particular location for broadscale upper-ocean variability in this region, we calculated the mean heat budget (0–250 m) in SODA and HYCOM averaged over the region (30°–10°S, 100°–80°W) where the largest annual mean low cloud cover is found (Colbo and Weller 2007; Table 2). We keep tenths of a unit for those estimates whose values are between -1 and $+1$ W m^{-2} to identify the sign. The results are consistent between the two models. First, cooling from geostrophic transport is large in both SODA and HYCOM. Second, warm advection resulting from Ekman transport is small, especially in SODA. Finally, the eddy heat flux divergence term is significantly small in both models and is negligible over this region. We have also examined the average over a few different boxes and find that the main conclusions are similar to those averaged in the box (30°–10°S, 100°–80°W) presented here.

We also computed these terms at 20°S, 85°W in the upper 50 m (Table 3), because horizontal heat advection and eddy heat flux divergence around 250 m may not directly affect SST, especially when the mixed layer is shallow. Heat advection resulting from Ekman transport at the IMET site is not much smaller than that resulting

TABLE 2. Ocean heat budget (0–250 m) averaged over the region (30°–10°S, 100°–80°W) from SODA and HYCOM. The periods for the averaging are January 1980–November 2005 for SODA and January 2003–April 2007 for HYCOM (units are W m^{-2}).

30°–10°S, 100°–80°W	Q_{net}	$-\mathbf{V}_{geo} \cdot \nabla T$	$-\mathbf{V}_{ek} \cdot \nabla T$	$-\nabla \cdot (\overline{\mathbf{V}'T'})$
SODA	—	−27	0.1	−0.4
HYCOM	11	−23	7	−1

from geostrophic transport because the Ekman currents are confined to the upper shallow layers. Eddy heat flux divergence provides a small cooling in SODA and a warming in HYCOM. If averaged over the entire stratus cloud deck region (30°–10°S, 100°–80°W; Table 4), Ekman heat advection in SODA is smaller than geostrophic heat advection. In addition, the area-averaged eddy heat flux divergence becomes negligible for both SODA and HYCOM. The role of eddies in the upper-ocean heat budget will be discussed further in section 4e.

4. Spatial distribution of the upper-ocean heat budget

In this section, the spatial distribution of major contributing terms, discussed in the previous section, is examined. We explore how geostrophic and Ekman transports and the divergence of eddy flux contribute to the upper-ocean heat budget by analyzing the model output in the entire stratus cloud deck region.

a. Net surface heat flux

The net surface heat flux computed from NOGAPS and HYCOM SST was averaged over the period 2003–07 (Fig. 3). It is positive (warming the ocean) over most of the region, including the IMET site (marked by an X on the map). Strong warming from the net surface heat flux is found near the coast, south of 15°S. This warming must be balanced by other processes, such as Ekman currents and strong coastal upwelling there. Over the open ocean, beneath the stratus cloud deck, the warming resulting from the net surface heat flux is weaker.

We also examined the net surface heat flux in the OAFlux (Yu and Weller 2007; Yu et al. 2008) and other atmospheric reanalyses (NCEP-1, NCEP-2, and ERA-40) to confirm that the spatial pattern is similar in other

TABLE 3. Ocean heat budget in the upper 50 m at the IMET site from SODA and HYCOM. The periods for the averaging are as in Table 2 (units are W m^{-2}).

(20°S, 85°W)	Q_{net}	$-\mathbf{V}_{geo} \cdot \nabla T$	$-\mathbf{V}_{ek} \cdot \nabla T$	$-\nabla \cdot (\overline{\mathbf{V}'T'})$
SODA	—	−6	4	−3
HYCOM	18	−10	−8	6

TABLE 4. Ocean heat budget in the upper 50 m averaged over the region (30°–10°S, 100°–80°W) from SODA and HYCOM. The periods for the averaging are as in Table 2 (units are W m^{-2}).

30°–10°S, 100°–80°W	Q_{net}	$-\mathbf{V}_{geo} \cdot \nabla T$	$-\mathbf{V}_{ek} \cdot \nabla T$	$-\nabla \cdot (\overline{\mathbf{V}'T'})$
SODA	—	−9	3	0.1
HYCOM	11	−5	6	−0.1

datasets (not shown). Net surface fluxes from all datasets show positive (warming of the ocean) in most of the stratus region, although there are some quantitative differences. This suggests that the surface heat fluxes used to force the model are appropriate for this particular study, which examines upper-ocean processes responsible for balancing the positive surface heat fluxes.

b. Geostrophic heat advection

Horizontal heat advection resulting from geostrophic currents was computed from the SODA and HYCOM output. Geostrophic currents are computed with respect to the ocean hydrography (i.e., the model temperature and salinity). Figure 4 shows temporal mean geostrophic heat advection and geostrophic currents and temperatures in the upper 50 m from SODA and HYCOM. The periods for the averaging are 1980–2005 for SODA and 2003–07 for HYCOM. It should be noted that we have also calculated the spatial distribution of this term as well as other terms in the heat equation using a period (2003–05) that both SODA and HYCOM cover and found that the results are similar.

In contrast to warming over most of the stratus cloud deck region from net surface heat flux, geostrophic transport causes significant upper-ocean cooling over
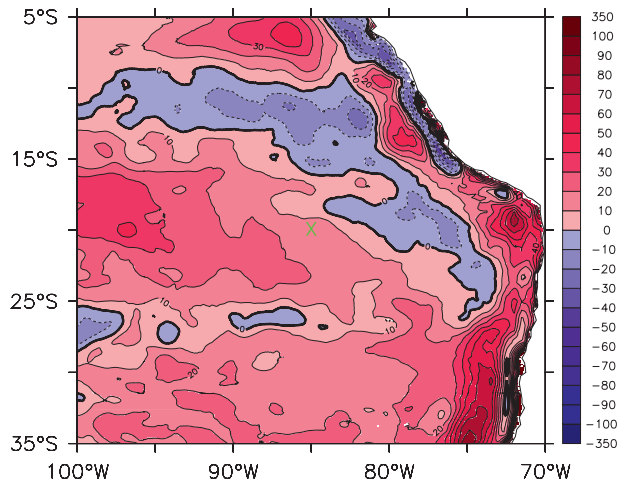

FIG. 3. Mean net surface heat flux (W m^{-2}; downward positive) based on NOGAPS and HYCOM SST averaged over 2003–07. The IMET site is marked by a green X on the map.
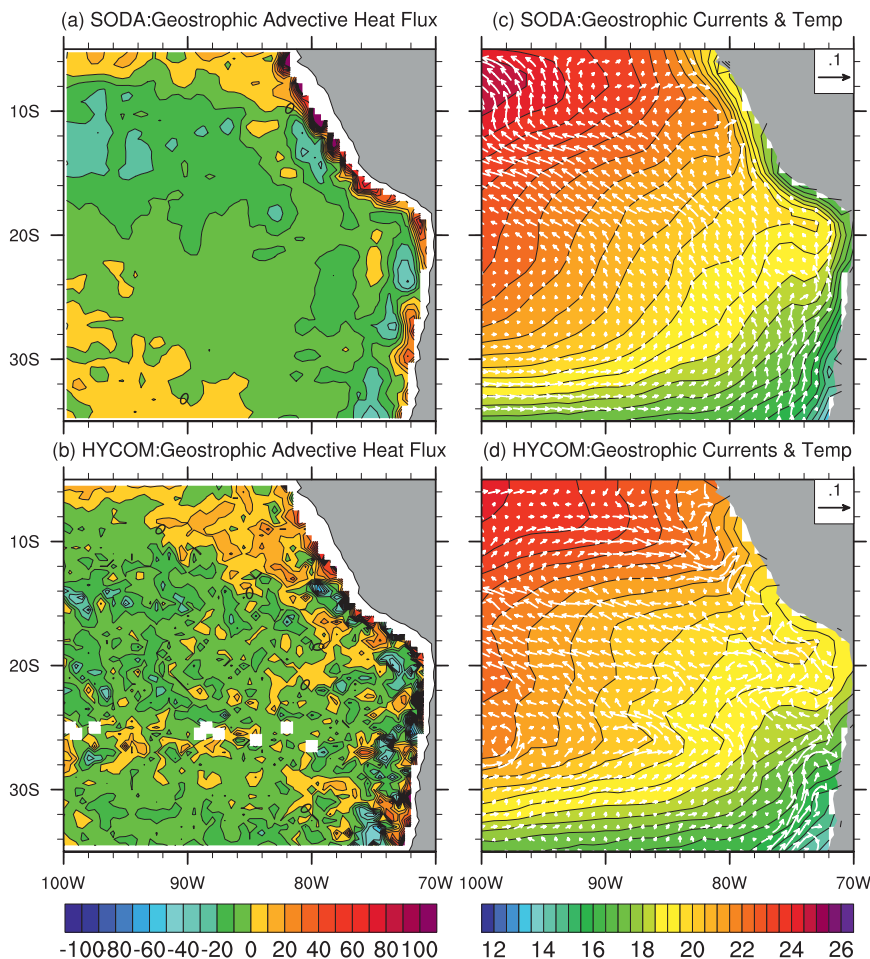
FIG. 4. (a) Mean geostrophic heat advection (W m^{-2}) and (c) mean geostrophic currents (m s^{-1}) and temperature (°C) in the upper 50 m from SODA. (b),(d) As in (a),(c), but from HYCOM. The periods for the averaging are January 1980–November 2005 for SODA and January 2003–April 2007 for HYCOM. The color bars (b),(d) are for geostrophic heat advection and temperature, respectively.

most of the stratus cloud deck region. The way in which geostrophic currents produce cooling is demonstrated by the map of temperature and geostrophic currents in SODA and HYCOM (Figs. 4c,d). Northwestward geostrophic currents in most of the stratus region cross the isotherms that are nearly perpendicular to the direction of the currents, and thus geostrophic currents transport cold water to the stratus cloud region. In some locations (e.g., in the region south of 30°S between 100° and 90°W), geostrophic currents flow along the isotherms and thus the heat transport resulting from geostrophic currents is negligible compared to that resulting from Ekman currents. However, overall in the region shown in Fig. 4, our analysis indicates that geostrophic transport plays an important role in the upper-ocean heat budget, which is consistent with Colbo and Weller's estimates using the IMET datasets (Colbo and Weller 2007).

To examine the uncertainty of annual mean geostrophic advective heat flux from SODA and HYCOM, we have also calculated this term using WOA05 temperature and salinity climatology (not shown). The magnitude and spatial pattern of this term based on the data agree with those from the models reasonably well. Geostrophic currents calculated from WOA05 data provide cooling most of the stratus cloud region. RMS difference with respect to the WOA05 data in the entire stratus cloud region (30°–10°S, 100°–80°W) is 5.7 W m^{-2} for SODA and 11.1 W m^{-2} for HYCOM.

c. Ekman transport of heat

Figure 5 shows the temporal mean Ekman heat transport and the temperature and Ekman currents from SODA and HYCOM in the upper 50 m. In SODA, the Ekman transport causes warming north of the IMET site
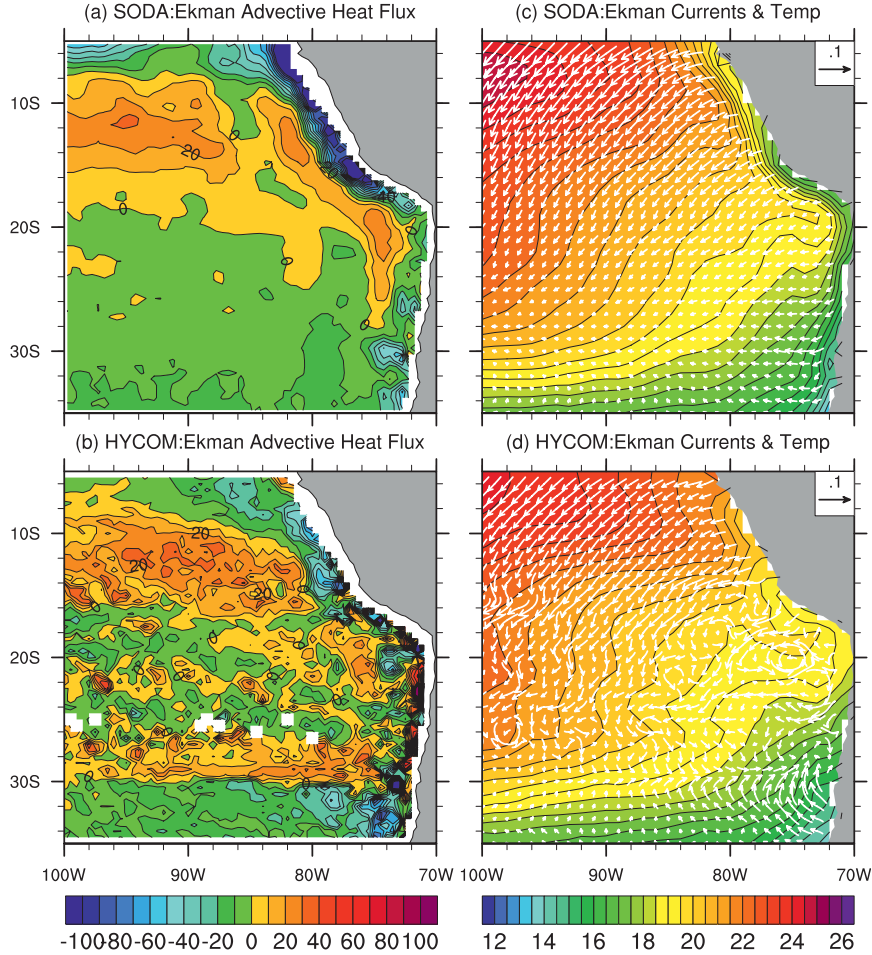
FIG. 5. As in Fig. 4, but for nongeostrophic transport (primarily Ekman transport) in the upper 50 m. The Ekman currents are approximated as the residual of total currents minus the geostrophic currents in this figure. The color bars are for (left) Ekman heat advection and (right) temperature.

and cooling south of the IMET site. Because the IMET site (20°S, 85°W) is located near the boundary between positive and negative heat advection, the magnitude of Ekman heat advection is minimal around this site. The overall spatial distribution of heat transport and the relation between currents and temperature in HYCOM are similar to those in SODA. However, there are more finescale structures in HYCOM in the region south of 16°S. It is unlikely that these fine structures are caused by the currents directly driven by local winds. In this study, however, we still retain the term "Ekman" while acknowledging these finescale features may not be the results of heat transport caused by currents directly generated by local winds.

To examine the uncertainty of Ekman advective heat flux from models, we have also computed Ekman heat transport from the WOA05 temperature climatology and ERA-40 wind stress climatology (not shown). The spatial pattern of Ekman advective heat flux calculated

from the data is very similar to that from the models, indicating that the large-scale features of this term are well captured by the models. RMS difference of annual mean values with respect to the WOA05 data in the stratus cloud region (30°–10°S, 100°–80°W) is 8.8 W m^{-2} for SODA and 11.7 W m^{-2} for HYCOM.

To examine whether the difference between total and geostrophic currents is a good approximation of Ekman currents, we also calculated Ekman transport directly using ERA-40 wind stress (1980–2001) and QuikSCAT wind stress (2002–2005) using

$$M_x = \frac{\tau_y}{\rho f} \quad \text{and}$$

$$M_y = -\frac{\tau_x}{\rho f}$$

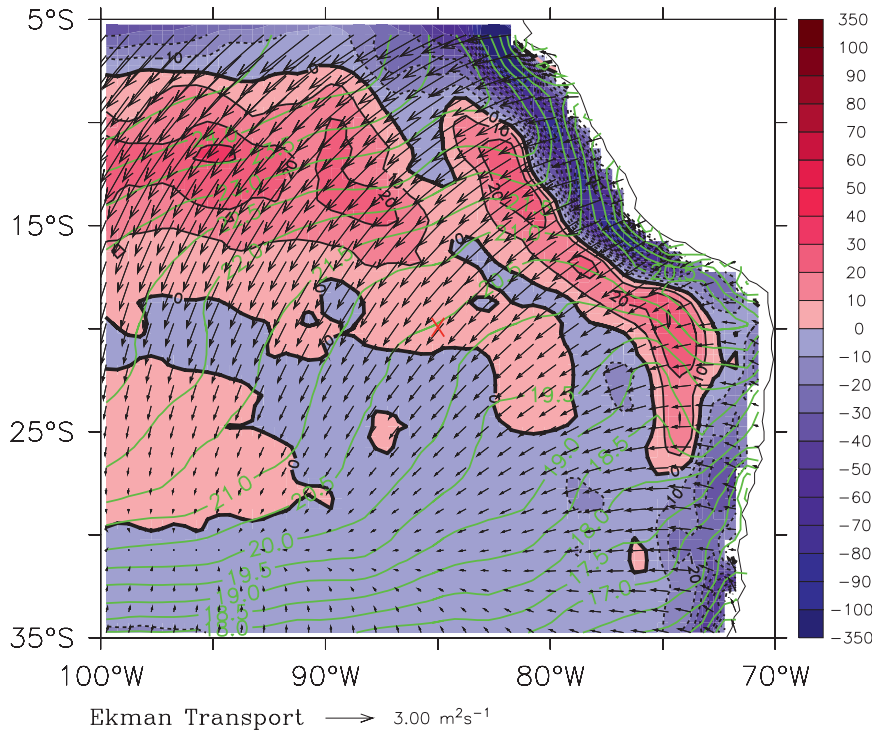as well as the Ekman advective heat flux with

FIG. 6. The mean advective heat flux in the mixed layer resulting from Ekman transport (black contours in W m^{-2}), mixed layer temperature (green contours in °C), and Ekman transport using ERA-40 wind stress (1980–2001) and QuikSCAT wind stress (2002–05; arrows in m^2 s^{-1}; from SODA).

$$H_{ek} = H_x + H_y = \frac{C_p \tau_y}{f}\frac{dT_{mld}}{dx} + \left(-\frac{C_p \tau_x}{f}\frac{dT_{mld}}{dy}\right),$$

where M_x and M_y are zonal and meridional Ekman transports, H_x and H_y are zonal and meridional Ekman advective heat flux, (τ_x, τ_y) are zonal and meridional wind stress from SODA, T_{mld} is mixed layer temperature in SODA, ρ is seawater density, $f = 2\Omega \sin\theta$ is the Coriolis parameter, and C_p is the specific heat capacity at constant pressure. The resulting Ekman transport and Ekman advective heat flux in the mixed layer averaged over 1980–2005 are shown in Fig. 6. Figure 6 also displays mixed layer temperature from SODA. Ekman advective heat flux in Fig. 6 is quite similar to that in Fig. 5a. Ekman transport causes net warming north of the IMET site and net cooling south of the IMET site. This provides justification for calculating Ekman heat advection using ageostrophic currents from the model output. The Ekman transport is nearly parallel to the mean SST isotherms in the offshore region near the IMET site, which is consistent with the result from Colbo and Weller (2007), although they used different datasets and a different analysis period.

d. Vertical heat advection

Figure 7a shows the vertical heat advection in the upper 50 m calculated from SODA. It is evident that vertical advection causes weak warming in the open ocean but not in the coastal region where strong upwelling occurs. The cooling resulting from the upwelling near the coast is balanced by the positive net surface heat flux (Fig. 3). Figure 7b shows the velocity and temperature section along 20°S. A pronounced vertical circulation centered around 40 m deep is evident at 78°W. Cold water upwelled near the coast is transported offshore by mean flow in the upper 40 m. Because of the downwelling caused by the convergence of surface currents in the open ocean, the weak subsurface warming occurs because of the vertical heat advection in broad areas of the stratus region.

It should be noted that the vertical heat advection in z coordinates is nontrivial to calculate reliably from the available HYCOM output. This is because HYCOM's natural coordinate system uses time-dependent hybrid layers rather than fixed z levels, and interpolated vertical velocities in z coordinates derived from the derivative of horizontal velocity at each level (layer) contain large errors.
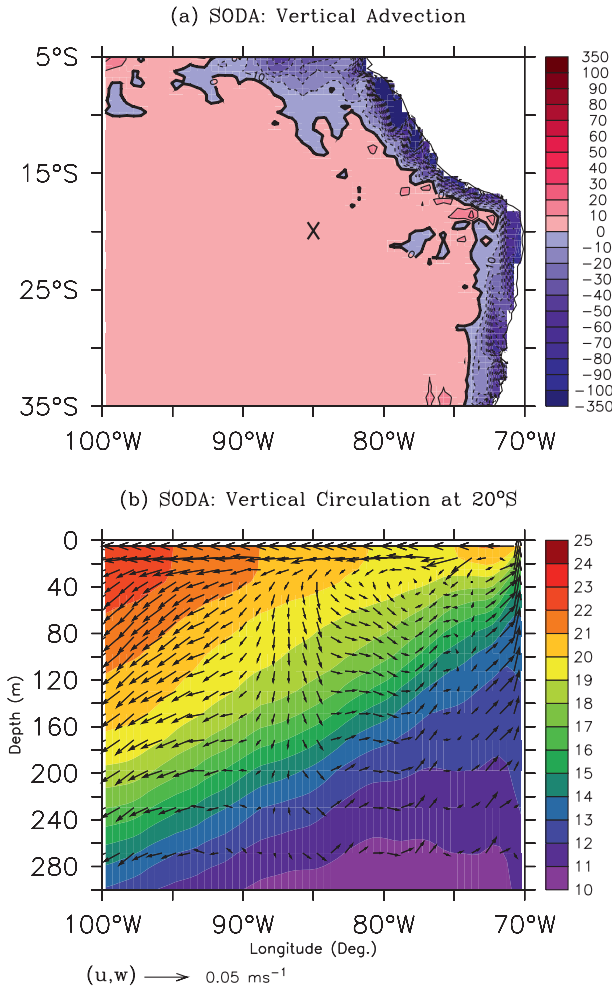
(a) SODA: Vertical Advection

(b) SODA: Vertical Circulation at 20°S

(u,w) ⟶ 0.05 ms^{-1}

FIG. 7. (a) Vertical heat advection (W m^{-2}) in the upper 50 m and (b) its ocean circulation (vectors in m s^{-1}) and temperature (shading contours in °C) in the zonal–vertical plane at 20°S averaged over 1980–2005 from SODA. The strong upwelling near the coast gives rise to cold vertical heat advection. Downward flow almost parallel to isotherm causes relatively weak warm vertical heat advection in the entire cloud deck region.

e. Eddy heat flux divergence

In this section, heat transport caused by eddies in models is discussed. We first compare eddy fields in models with those in satellite observations to examine whether models are able to generate realistic eddies in this region. Then eddy heat flux divergence is computed in the entire stratus cloud region to identify the role of eddies in overall heat balance in this region.

1) EDDY KINETIC ENERGY

Eddy activity in models is examined by calculating eddy kinetic energy (EKE). To demonstrate how well the models can generate realistic eddies, we compare EKE from models with that derived from satellite al-

timeters (i.e., AVISO surface geostrophic velocity). HYCOM's surface geostrophic velocity is first averaged onto a $\frac{1}{3}° \times \frac{1}{3}°$ grid to match the spatial resolution of AVISO geostrophic velocity. Then, EKE is computed as EKE $= (u_{geo}'^2 + v_{geo}'^2)/2$, where $u_{geo}'^2$ and $v_{geo}'^2$ are deviations of the 5-day-averaged geostrophic velocity from its seasonally averaged values. Data on a $0.5° \times 0.5°$ grid are used for SODA. Figure 8 shows the map of annual mean surface EKE (cm^2 s^{-2}) from SODA, HYCOM, and AVISO. The magnitude and spatial pattern of EKE in HYCOM are similar to those from observations. In HYCOM and observations, eddies are more active near the coastal region than in the open ocean (Figs. 8b,c). Because HYCOM uses sufficiently fine horizontal resolution to resolve mesoscale eddies, its overall eddy activity is much higher than that in SODA, which uses a relatively coarse resolution. Despite the general agreement between HYCOM and observations, there are some notable differences. For example, EKE in HYCOM is larger than observations near the coast. In the open ocean, particularly in the region of 20°–15°S, 100°–90°W, the EKE is higher than observations.

Eddy activity in the southeast Pacific Ocean has been also reported in some previous studies (Hormazabal et al. 2004; Chaigneau and Pizarro 2005a,b; Penven et al. 2005). The spatial distribution and magnitude of mean EKE in HYCOM shown in Fig. 8 are similar to those derived from drifter data (Chaigneau and Pizarro 2005a) and satellite altimeter data (Hormazabal et al. 2004; Penven et al. 2005). The good agreement of eddy fields between HYCOM and observations suggests that the HYCOM output is suitable for examining the role of eddies in the upper-ocean heat budget in this region.

The enhanced eddy activity along the coast can be explained by many processes. For instance, the interaction of the Peru–Chile Current system with the coastline is able to produce the active eddies (Chaigneau and Pizarro 2005a). Coastal flows with large interannual and seasonal variability are relevant to disturbances of equatorial origin that may reinforce the unstable coastal jet (Pizarro et al. 2002; Zamudio et al. 2006, 2007). Also the strong upwelling fronts observed in spring and summer could generate baroclinic instabilities that may enhance mesoscale variability. Furthermore, downwelling coastal Kelvin waves can strongly intensify the Peru–Chile Undercurrent system (Shaffer et al. 1997), which may destabilize the near-surface-coastal circulation-generating eddies.

It should be noted that EKE in AVISO data is computed from the deviation of surface geostrophic velocity, which could be much weaker than the total velocity deviation. We also calculated the EKE using total velocities from SODA and HYCOM [i.e., EKE $= (u'^2 + v'^2)/2$,
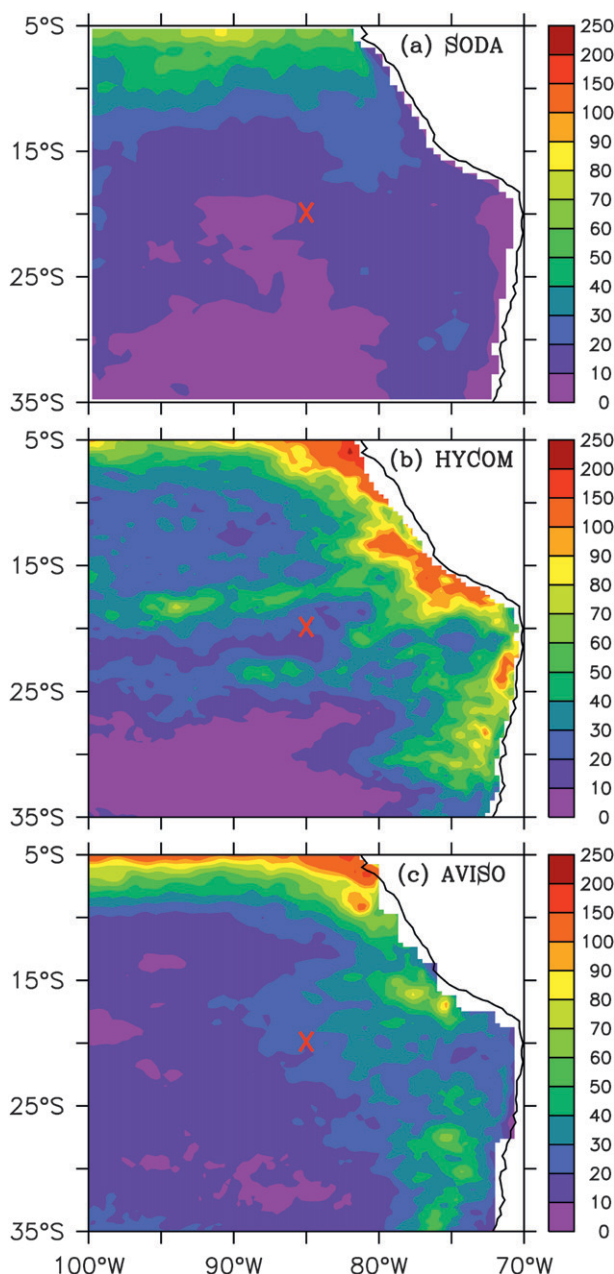
FIG. 8. Maps of eddy activity represented by the temporal mean of surface EKE derived from geostrophic velocity for (a) SODA, (b) HYCOM, and (c) AVISO. The periods for averages are 1980–2005 for SODA, 2003–07 for HYCOM, and 22 Aug 2001–28 Feb 2009 for AVISO. The primed terms are deviations from seasonally averaged values. Units are cm^2 s^{-2}.
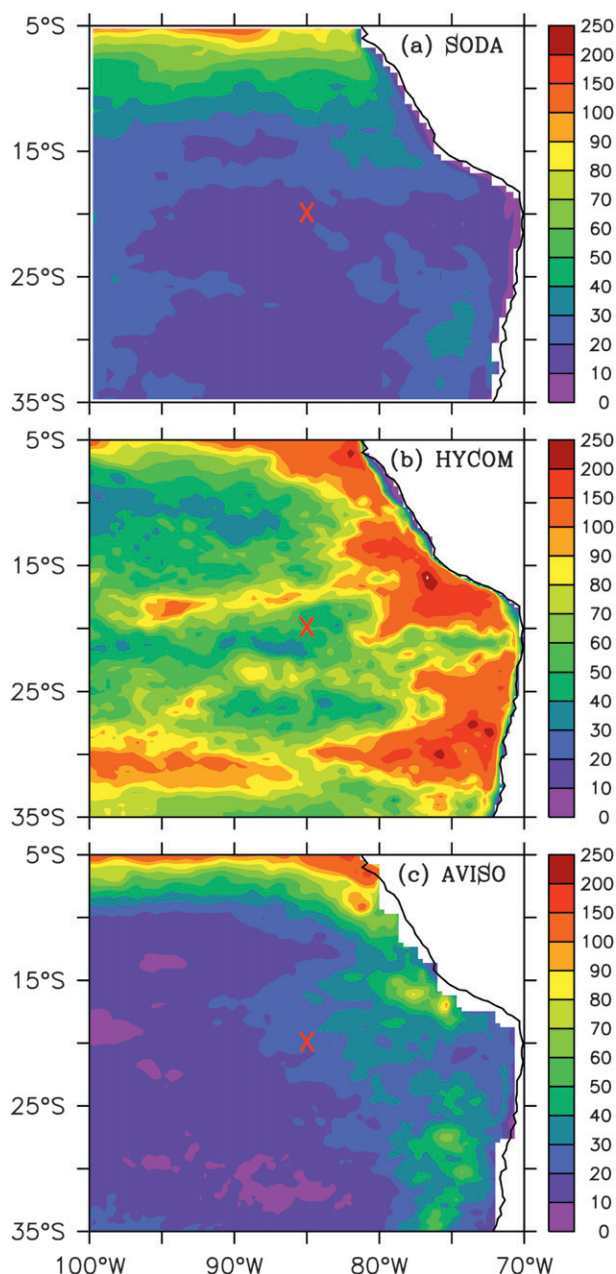
FIG. 9. As in Fig. 8, but the EKE is computed using the total velocity for (a) SODA and (b) HYCOM. (c) AVISO remains the same as in Fig. 8c.

where u' and v' are deviations of the total velocity from their seasonally averaged values]. Figure 9 illustrates the annual mean of EKE derived from the total velocity. The EKE values in SODA and HYCOM are significantly higher in both the open ocean and near the coast than those derived from geostrophic velocity. This sug-

gests that the eddy kinetic energy calculated from AVISO data can be underestimated, because only a geostrophic component of velocity field is used.

2) EDDY CHARACTERISTICS

To further illustrate the characteristics of eddies simulated in HYCOM, the vertical component of vorticity and the Okubo–Weiss parameter (OWP) at 30-m depth were computed. Figures 10a,d show HYCOM temperatures
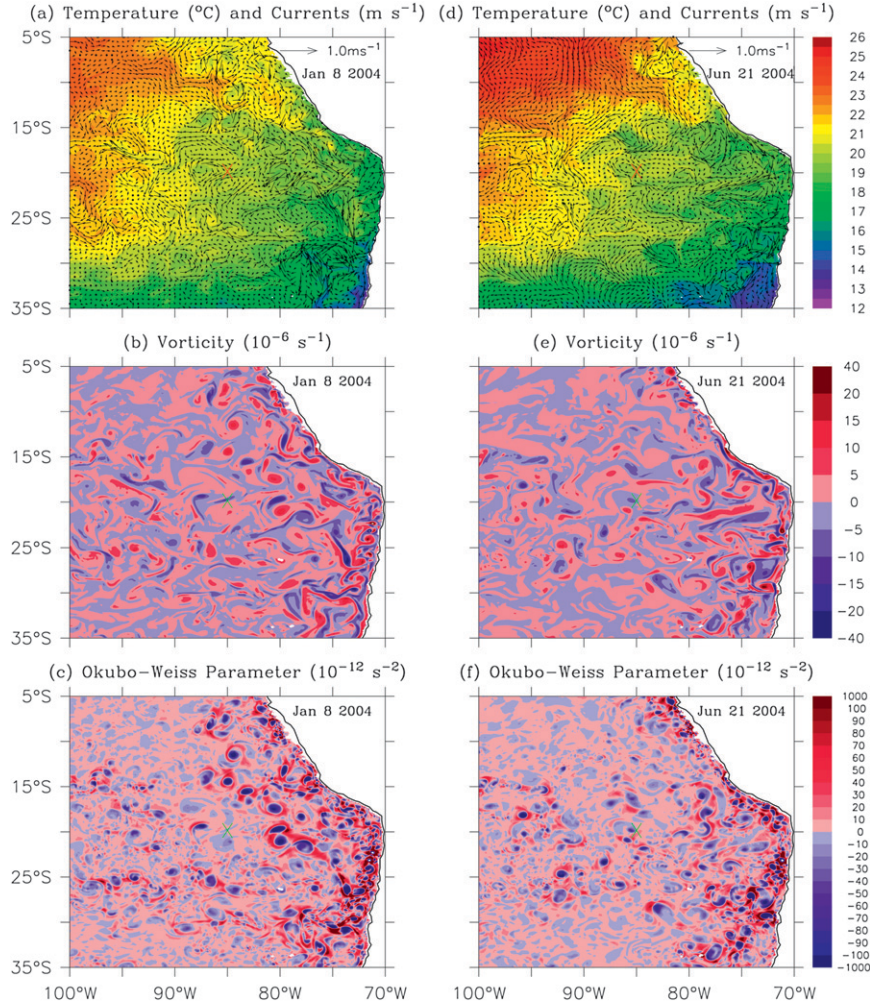
FIG. 10. Ocean states at 30 m in HYCOM on two dates. (a) Temperature (shading contours in °C) and currents (vectors in m s^{-1}), (b) relative vorticity (in 10^{-6} s^{-1}), and (c) OWP (10^{-12} s^{-2}) on 8 Jan 2004. (d),(e),(f) As in (a),(b),(c), but on 21 Jun 2004. The color bars on right are for (top) temperature, (middle) vorticity, and (bottom) OWP.

(in °C) and currents (in m s^{-1}) at 30-m depth in the southeast Pacific Ocean associated with the mesoscale ocean eddy field on 8 January and 21 June 2004. OWPs on these dates are also shown in Figs. 10c,f. The OWP is defined as

$$\text{OWP} = \left(\frac{\partial u}{\partial x} - \frac{\partial v}{\partial y}\right)^2 + \left(\frac{\partial v}{\partial x} + \frac{\partial u}{\partial y}\right)^2 - \left(\frac{\partial v}{\partial x} - \frac{\partial u}{\partial y}\right)^2,$$

where u and v are the horizontal velocity components and x and y are the horizontal coordinates. The first two terms on the right-hand side represent the deformation and the last term is the vertical component of the relative vorticity. If OWP is positive (negative), the deformation (relative vorticity) dominates. Therefore, the OWP helps identify the boundary of eddies, because

eddies are generally characterized by a strong rotation in their center and a strong deformation in their periphery. Thus, eddies can be demonstrated by patches of negative values of OWP surrounded by positive rings. The snapshot of subsurface vorticity (Figs. 10b,e) indicates a succession of cyclones and anticyclones, which is generated at the upwelling front. Eddies are clearly seen in the image of the OWP (Figs. 10c,f). They appear more energetic near the coastal area. In the open ocean, including near the IMET site, the eddies clearly exist, although they are relatively weaker. These spatial distributions are consistent with the spatial pattern of the EKE.

3) EXAMPLE OF COLD-CORE EDDIES

Colbo and Weller (2007) speculated that the cooling at the IMET site resulting from eddy heat flux divergence is
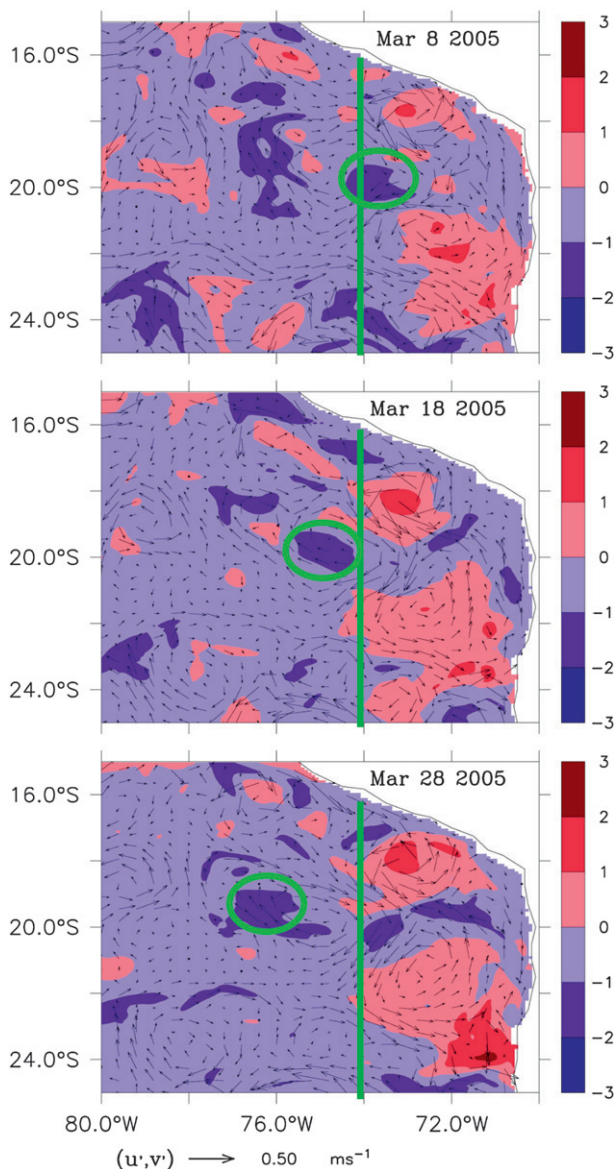
FIG. 11. Maps of temperature anomalies (shaded contours in °C) along with velocity anomaly vectors (arrows in m s^{-1}) averaged in the upper 50 m during (top) 8, (middle) 18, and (bottom) 28 March 2005 are illustrated for the evolution of cyclonic eddies (i.e., cold eddy) in HYCOM. The offshore propagation of a cold eddy is marked by green ellipses. Anomalies of temperature and velocity are derived from the 2003–07 pentad climatology.

likely to be caused by the cold-core eddies that have been advected offshore from the upwelling region where these eddies are generated. To identify such cold eddies in HYCOM, temperature and velocity anomalies during the entire period of the experiment are inspected.

Figure 11 shows the maps of temperature and velocity anomalies averaged in the upper 50 m during March 2005. The anomalies of temperature and velocity are derived from the 2003–07 pentad climatology. Many
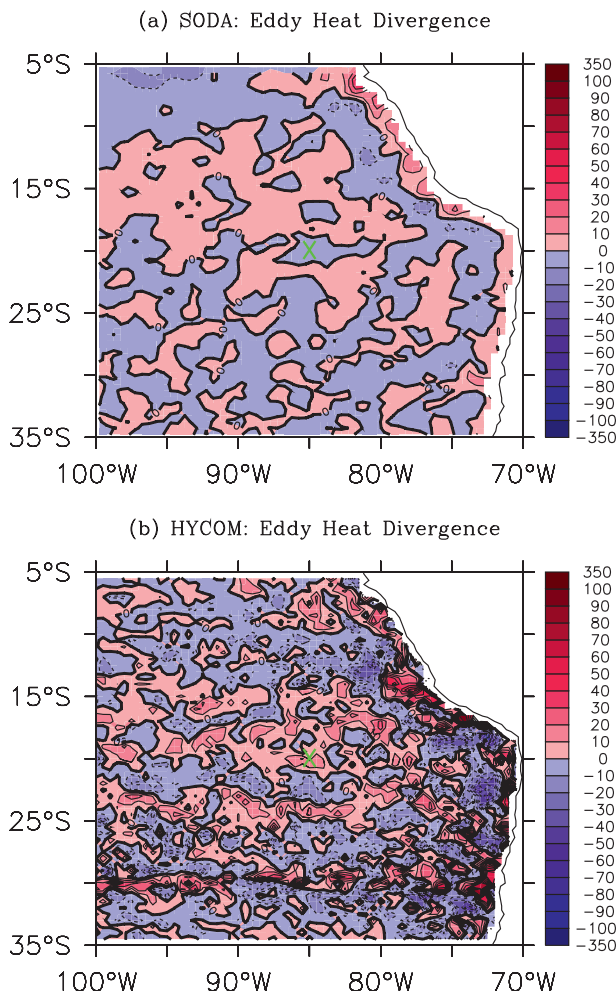
FIG. 12. Maps of mean eddy heat flux divergence in the upper 50 m for (a) SODA and (b) HYCOM (units are W m^{-2}).

anticyclonic (cyclonic) eddies associated with warm (cold) waters are found near the coast. During this period, an eddy associated with cold waters and cyclonic circulation around 20°S, 74°W on 8 March propagates westward and reaches around 76°W on 28 March. Similar westward-propagating cold-core cyclonic eddies are frequently found in HYCOM. However, these cyclonic eddies associated with cold waters in the upper layer are mostly found within several degrees away from the coastline and seldom propagate to locations near the IMET site during the period of model experiment.

4) ROLES OF EDDY HEAT FLUX

The eddy heat flux divergence is computed following the definition $-(\partial u'T'/\partial x + \partial v'T'/\partial y)$, where u', v', and T' are deviations of the total velocity and temperature (5-day averaged) from their seasonally averaged values. Figure 12 shows the spatial distribution of mean eddy

heat flux divergence in the upper 50 m from SODA and HYCOM. Because of the weak eddy activity in SODA, the eddy flux divergence is very small in the entire stratus region. The magnitude of eddy flux divergence in HYCOM is much larger than that in SODA, particularly near the coast. Near the IMET site, the temporal mean of eddy heat flux in HYCOM is positive ($+6$ W m^{-2}), which could be significant at this location. However, unlike geostrophic and Ekman heat transports, the eddy flux divergence term is not spatially coherent. As a result, the temporal mean of eddy heat flux averaged over 30°–10°S, 100°–80°W is much smaller (see Tables 2, 4) than the estimate by Colbo and Weller (2007) at the IMET site. Therefore, the overall impact from eddy flux divergence on the upper-ocean heat budget in the stratus cloud region is negligible in contrast to geostrophic and Ekman transports, which are spatially more coherent.

The results are consistent with the inspection of individual eddies in HYCOM, which shows that cold waters generated near the upwelling region do not often move with eddies far west into the open ocean, including toward the IMET site. Although the westward propagation of cyclonic eddies from the coast to the open ocean is often found in HYCOM, cold surface waters generated near the coast are not carried very far by these cyclonic eddies, and thus they do not significantly impact overall heat balance in the open ocean.

Our result in spatial pattern of the eddy heat flux divergence in the 50-m surface layer is similar to that in a previous observational study by Chaigneau and Pizarro (2005a), who used Fickian law to estimate the eddy heat flux divergence, in which the *World Ocean Atlas 2001* (WOA01) temperatures are used and the zonal and meridional components of eddy diffusivity are estimated based on the drifter trajectories. Even though using Fickian law may not be quite appropriate to describe the eddy heat flux divergence resulting from coherent mesoscale eddies, we did not detect a significant deviation in this case, suggesting that their results are useful here. In their study, the area-averaged eddy heat flux divergence (34°–10°S, 100°–70°W) provides heat to the surface layer at a rate of $+4.4$ W m^{-2}. Such eddy flux divergence should be much smaller if averaged over the stratus region (34°–10°S, 100°–80°W) because the eddy flux divergence near the coast is much larger than the open ocean. The small value of eddy heat flux divergence is primarily due to its spatial incoherence.

Cold waters near the surface associated with eddies can be modified by surface heat fluxes and quickly resemble the rest of the upper mixed layer. Thus, cold waters in lower portions of the eddies may be observable farther from the coast, because they are insulated from

TABLE 5. Ocean heat budget in the upper 50 m averaged over the regions (20°–10°S, 100°–80°W) and (30°–20°S, 100°–80°W) from SODA and HYCOM. The periods for the averaging are as in Table 2 (units are W m^{-2}).

20°–10°S, 100°–80°W	Q_{net}	$-\mathbf{V}_{geo} \cdot \nabla T$	$-\mathbf{V}_{ek} \cdot \nabla T$	$-\nabla \cdot (\overline{\mathbf{V}'T'})$
SODA	—	−13	9	0.4
HYCOM	7	−6	10	−0.2
30°–20°S, 100°–80°W				
SODA	—	−4	−3	−0.2
HYCOM	14	−5	2	0.1

the atmosphere. In this case, water masses below 50 m associated with eddies could possibly influence upper-ocean heat balance in the open ocean. To examine such a possibility, we also computed the eddy heat flux divergence in the upper 250 m from SODA and HYCOM (not shown). The results are similar to those in the upper 50 m, in which the eddy heat flux divergence term is not spatially coherent, although typically the magnitude at a given location is larger, because it is integrated through a deeper layer.

5. Discussion

The spatial distribution of horizontal heat advection resulting from Ekman transport (Fig. 5) indicates that it causes warming (cooling) to the north (south) of around 20°S in the stratus deck region. We have also calculated the area average of each term north and south of 20°S (Table 5). Heat advection resulting from Ekman transport gives stronger warming in the northern part of the stratus cloud region. To the south of this region, this warming becomes much weaker in HYCOM or changes the sign in SODA. Cooling resulting from geostrophic transport is evident in both north and south regions, but it is weaker in the south for SODA. As indicated in the spatial distribution of the eddy heat flux divergence term, this term is negligible both north and south of 20°S. Accordingly, the contribution of each term can be very different in northern and southern parts of the stratus region; thus, additional observations such as surface buoys in locations both south and north of 20°S will help improve our understanding of upper-ocean processes under the stratus cloud decks in the southeast Pacific.

There are other terms in the heat equation that are not discussed in detail. The major additional term that could significantly contribute to the heat budget is vertical diffusion (mixing). Although this term is negligible at 250-m depth (Colbo and Weller 2007), it could be comparable to other terms in the 0–50-m layer. Unfortunately, it is difficult to estimate this term accurately

at 50 m from the available model output. We have also performed the same analyses in this paper for the 0–250-m layer in which the vertical diffusion term is negligible, showing that the spatial distribution of horizontal heat advection and eddy heat flux divergence terms for the 0–250-m layer are similar to those for the 0–50-m layer (not shown). However, it is possible that the vertical mixing term could contribute to the closure of the heat budget for the 0–50-m layer.

Although the analysis of HYCOM output indicates that the eddy flux divergence term is negligible in the heat budget of the entire stratus deck region in comparison to horizontal advection terms, the result could be model dependent. Also, HYCOM was integrated for only 4 yr, and it is possible that the result could be different in other time periods. In fact, large interannual variations within the upper ocean associated with ENSO are evident in the stratus cloud region (Shinoda and Lin 2009). Longer integrations using multiple eddy-resolving models are necessary to further investigate the role of eddies in this region.

6. Summary

This study examines the upper-ocean processes in the stratus cloud deck region using SODA data and the eddy-resolving HYCOM. The model performance is first evaluated based on comparison with in situ data from the IMET buoy at 20°S, 85°W. Then, the annual mean of the upper-ocean heat budget is calculated from the model output. The relative importance of physical processes responsible for the heat budget is also investigated, particularly the roles of geostrophic and Ekman transports and the eddy heat flux. The analysis of model output was conducted for the entire stratus cloud deck region to examine the representativeness of the IMET observation site for broadscale upper-ocean processes in this region.

Both SODA and HYCOM reproduce the seasonal evolution of the mixed layer reasonably well. The mean heat budget for the upper 250 m in the models is compared with the corresponding heat budget based on observations at 20°S, 85°W, and it demonstrates some consistencies. Net surface heat fluxes used in the HYCOM experiment provide warming in most areas of the stratus deck, including the IMET mooring site. One of the major sources of cooling that balances the positive surface heat fluxes is geostrophic transport. These results are consistent with those from observations described in Colbo and Weller (2007).

Major terms of the heat equation in the upper 50 m were also calculated over a large portion of the stratus region. The heat transport produced by mean geostrophic currents is one of the primary sources of cooling in the entire stratus region because of its spatial coherence. Although Ekman currents are generally stronger than geostrophic currents in the upper 50 m, heat transport resulting from geostrophic currents is comparable to that by Ekman currents. This is because the direction of geostrophic currents in this region is nearly perpendicular to the isotherms of the upper-ocean temperature, whereas Ekman currents are nearly parallel to the isotherms. It is found that Ekman transport generates warming (cooling) to the north (south) of around 20°S. This result is consistent with the estimates by Colbo and Weller (2007) in which Ekman heat transport is negligible at the IMET site (20°S, 85°W).

The role of eddies in the upper-ocean heat budget is examined using the eddy-resolving HYCOM and observational data. A comparison of eddy activity in HYCOM with that derived from satellite observations (i.e., AVISO) indicates that HYCOM is capable of simulating the realistic eddies in the stratus cloud region. The results indicate that the eddy heat flux divergence term is negligible for the entire stratus region because it is not spatially coherent, although it could be comparable to other terms at a particular location.

A substantial amount of data in the upper ocean and atmospheric boundary layer has been collected recently in the region of stratus cloud deck in the southeast Pacific during the VAMOS Ocean-Cloud-Atmosphere-Land Study (VOCALS) Regional Experiment (VOCALS REx; Wood et al. 2007). In the next few years, thorough analyses of these datasets will be conducted by many investigators. Hopefully, knowledge of the upper-ocean heat budget obtained in this study will help interpret the results of their analyses.

REFERENCES

Bingham, F. M., S. D. Howden, and C. J. Koblinsky, 2002: Sea surface salinity measurements in the historical database. *J. Geophys. Res.,* **107,** 8019, doi:10.1029/2000JC000767.

Bleck, R., 2002: An oceanic general circulation model framed in hybrid isopycnic-Cartesian coordinates. *Ocean Modell.,* **4,** 55–88.

——, and D. B. Boudra, 1981: Initial testing of a numerical ocean circulation model using a hybrid (quasi-isopycnic) vertical coordinate. *J. Phys. Oceanogr.,* **11,** 755–770.

——, and S. G. Benjamin, 1993: Regional weather prediction with a model combining terrain-following and isentropic coordinates. Part I: Model description. *Mon. Wea. Rev.,* **121,** 1770–1785.

Boyer, T. P., C. Stephens, J. I. Antonov, M. E. Conkright, L. A. Locarnini, T. D. O'Brien, and H. E. Garcia, 2002: *Salinity.* Vol. 2, *World Ocean Atlas 2001,* NOAA Atlas NESDIS 49, 165 pp.

Bradley, E. F., C. W. Fairall, J. E. Hare, and A. A. Grachev, 2000: An old and improved bulk algorithm for air-sea fluxes. Preprints, *14th Symp. on Boundary Layer and Turbulence,* Aspen, CO, Amer. Meteor. Soc., 294–296.

Carton, J. A., and B. S. Giese, 2008: A reanalysis of ocean climate using Simple Ocean Data Assimilation (SODA). *Mon. Wea. Rev.,* **136,** 2999–3017.

——, G. A. Chepurin, X. Cao, and B. S. Giese, 2000a: A Simple Ocean Data Assimilation analysis of the global upper ocean 1950–95. Part I: Methodology. *J. Phys. Oceanogr.,* **30,** 294–309.

——, ——, and ——, 2000b: A Simple Ocean Data Assimilation analysis of the global upper ocean 1950–95. Part II: Results. *J. Phys. Oceanogr.,* **30,** 311–326.

Chaigneau, A., and O. Pizarro, 2005a: Mean surface circulation and mesoscale turbulent flow characteristics in the eastern South Pacific from satellite tracked drifters. *J. Geophys. Res.,* **110,** C05014, doi:10.1029/2004JC002628.

——, and ——, 2005b: Eddy characteristics in the eastern South Pacific. *J. Geophys. Res.,* **110,** C06005, doi:10.1029/2004JC002815.

Colbo, K., and R. Weller, 2007: The variability and heat budget of the upper ocean under the Chile-Peru stratus. *J. Mar. Res.,* **65,** 607–637.

Diaz, H., C. Folland, T. Manabe, D. Parker, R. Reynolds, and S. Woodruff, 2002: Workshop on advances in the use of historical marine climate data. *WMO Bull.,* **51,** 377–380.

Gordon, C. T., A. Rosati, and R. Gudgel, 2000: Tropical sensitivity of a coupled model to specified ISCCP low clouds. *J. Climate,* **13,** 2239–2260.

Han, W., 2005: Origins and dynamics of the 90-day and 30–60-day variations in the equatorial Indian Ocean. *J. Phys. Oceanogr.,* **35,** 708–728.

——, T. Shinoda, L.-L. Fu, and J. P. McCreary, 2006: Impact of atmospheric intraseasonal oscillations on the Indian Ocean dipole. *J. Phys. Oceanogr.,* **36,** 670–690.

Hormazabal, S., G. Shaffer, and O. Leth, 2004: Coastal transition zone off Chile. *J. Geophys. Res.,* **109,** C01021, doi:10.1029/2003JC001956.

Hurlburt, H. E., E. J. Metzger, P. J. Hogan, C. E. Tilburg, and J. F. Shriver, 2008: Steering of upper ocean currents and fronts by the topographically constrained abyssal circulation. *Dyn. Atmos. Oceans,* **45,** 102–134.

Jones, P. W., 1999: First- and second-order conservative remapping schemes for grids in spherical coordinates. *Mon. Wea. Rev.,* **127,** 2204–2210.

Kalnay, E., and Coauthors, 1996: The NCEP/NCAR 40-Year Reanalysis Project. *Bull. Amer. Meteor. Soc.,* **77,** 437–471.

Kara, A. B., H. E. Hurlburt, and A. J. Wallcraft, 2005a: Stability-dependent exchange coefficients for air–sea fluxes. *J. Atmos. Oceanic Technol.,* **22,** 1080–1094.

——, A. J. Wallcraft, and H. E. Hurlburt, 2005b: A new solar radiation penetration scheme for use in ocean mixed layer studies: An application to the Black Sea using a fine-resolution Hybrid Coordinate Ocean Model (HYCOM). *J. Phys. Oceanogr.,* **35,** 13–32.

——, ——, and ——, 2005c: Sea surface temperature sensitivity to water turbidity from simulations of the turbid Black Sea using HYCOM. *J. Phys. Oceanogr.,* **35,** 33–54.

Klein, S. A., and D. L. Hartmann, 1993: The seasonal cycle of low stratiform clouds. *J. Climate,* **6,** 1587–1606.

Large, W. G., J. C. McWilliams, and S. C. Doney, 1994: Oceanic vertical mixing: Review and model with a nonlocal boundary layer parameterization. *Rev. Geophys.,* **32,** 363–403.

Lin, J. L., 2007: The double-ITCZ problem in IPCC AR4 coupled GCMs: Ocean–atmosphere feedback analysis. *J. Climate,* **20,** 4497–4525.

Ma, C.-C., C. R. Mechoso, A. W. Robertson, and A. Arakawa, 1996: Peruvian stratus clouds and the tropical Pacific circulation: A coupled ocean–atmosphere GCM study. *J. Climate,* **9,** 1635–1645.

Mechoso, C. R., and Coauthors, 1995: The seasonal cycle over the tropical Pacific in coupled ocean–atmosphere general circulation models. *Mon. Wea. Rev.,* **123,** 2825–2838.

Miller, R. L., 1997: Tropical thermostats and low cloud cover. *J. Climate,* **10,** 409–440.

Penven, P., V. Echevin, J. Pasapera, F. Colas, and J. Tam, 2005: Average circulation, seasonal cycle, and mesoscale dynamics of the Peru Current System: A modeling approach. *J. Geophys. Res.,* **110,** C10021, doi:10.1029/2005JC002945.

Pizarro, O., G. Shaffer, B. Dewitte, and M. Ramos, 2002: Dynamics of seasonal and interannual variability of the Peru-Chile Undercurrent. *Geophys. Res. Lett.,* **29,** 1581, doi:10.1029/2002GL014790.

Rosmond, T. E., J. Teixeira, M. Peng, T. F. Hogan, and R. Pauley, 2002: Navy Operational Global Atmospheric Prediction System (NOGAPS): Forcing for ocean models. *Oceanography,* **15,** 99–108.

Shaffer, G., O. Pizarro, L. Djurfeldt, S. Salinas, and J. Rutlant, 1997: Circulation and low-frequency variability near the Chile coast: Remotely forced fluctuations during the 1991–92 El Niño. *J. Phys. Oceanogr.,* **27,** 217–235.

Shaji, C., C. Wang, G. R. Halliwell Jr., and A. Wallcraft, 2005: Simulation of tropical Pacific and Atlantic Oceans using a hybrid coordinate ocean model. *Ocean Modell.,* **9,** 253–282.

Shinoda, T., and J. L. Lin, 2009: Interannual variability of the upper ocean in the southeast Pacific stratus cloud region. *J. Climate,* **22,** 5072–5088.

——, P. E. Roundy, and G. E. Kiladis, 2008: Variability of intraseasonal Kelvin waves in the equatorial Pacific Ocean. *J. Phys. Oceanogr.,* **38,** 921–944.

Simmons, A. J., and J. K. Gibson, 2002: The ERA-40 project plan. ECMWF ERA-40 Project Rep. Series 1, 63 pp.

Smith, R. D., J. K. Dukowicz, and R. C. Malone, 1992: Parallel ocean general circulation modeling. *Physica D,* **60,** 38–61.

Stephens, C., J. I. Antonov, T. P. Boyer, M. E. Conkright, R. A. Locarnini, T. D. O'Brien, and H. E. Garcia, 2002: *Temperature.* Vol. 1, *World Ocean Atlas 2001,* NOAA Atlas NESDIS 49, 169 pp.

Wood, R., C. Bretherton, B. Huebert, C. R. Mechoso, and R. Weller, 2007: The VAMOS Ocean-Cloud-Atmosphere-Land Study (VOCALS): Improving understanding, model simulations, and prediction of the southeast Pacific climate system. Post-VOCALS-Rex Rep. [Available online at http://www.eol.ucar.edu/projects/vocals/.]

Xie, S.-P., 2004: The shape of continents, air-sea interaction, and the rising branch of the Hadley circulation. *The Hadley Circulation: Present, Past and Future,* H. F. Diaz and R. S. Bradley, Eds., Kluwer Academic, 121–152.

Yu, L., and R. A. Weller, 2007: Objectively analyzed air–sea fluxes for the global ice-free oceans (1981–2005). *Bull. Amer. Meteor. Soc.,* **88,** 527–539.

——, X. Jin, and R. A. Weller, 2008: Multidecade global flux datasets from the Objectively Analyzed Air-Sea Fluxes (OAFlux) Project: Latent and sensible heat fluxes, ocean evaporation, and related surface meteorological variables. Woods Hole Oceanographic Institution OAFlux Project Tech. Rep. OA-2008-01, 64 pp.

Zamudio, L., H. E. Hurlburt, E. J. Metzger, S. L. Morey, J. J. O'Brien, C. Tilburg, and J. Zavala-Hidalgo, 2006: Interannual variability of Tehuantepec eddies. *J. Geophys. Res.,* **111,** C05001, doi:10.1029/2005JC003182.

——, ——, ——, and C. E. Tilburg, 2007: Tropical wave-induced oceanic eddies at Cabo Corrientes and the María Islands, Mexico. *J. Geophys. Res.,* **112,** C05048, doi:10.1029/2006JC004018.

Zheng, Y., and B. S. Giese, 2009: Ocean heat transport in Simple Ocean Data Assimilation: structure and mechanisms. *J. Geophys. Res.,* **114,** C11009, doi:10.1029/2008JC005190.